

Demonstration of high-performance compact magnetic shields for chip-scale atomic devices

E. A. Donley, E. Hodby, L. Hollberg, and J. Kitching

Time and Frequency Division, National Institute of Standards and Technology, 325 Broadway, Boulder, Colorado 80305

(Received 9 May 2007; accepted 8 July 2007; published online 14 August 2007)

We have designed and tested a set of five miniature nested magnetic shields constructed of high-permeability material, with external volumes for the individual shielding layers ranging from 0.01 to 2.5 cm³. We present measurements of the longitudinal and transverse shielding factors (the ratio of external to internal magnetic field) of both individual shields and combinations of up to three layers. The largest shielding factor measured was 6×10^6 for a nested set of three shields, and from our results we predict a shielding factor of up to 1×10^{13} when all five shields are used. Two different techniques were used to measure the internal field: a chip-scale atomic magnetometer and a commercially available magnetoresistive sensor. Measurements with the two methods were in good agreement. © 2007 American Institute of Physics. [DOI: 10.1063/1.2767533]

I. INTRODUCTION

Many instruments based on atomic spectroscopy, such as atomic clocks¹⁻³ or NMR gyroscopes,⁴⁻⁶ are sensitive to magnetic fields. Stray magnetic fields and field fluctuations cause shifts of the atomic transition frequencies, which can lead to reduced stability. To achieve their performance potential, it is necessary to reduce the magnetic field sensitivity of chip-scale atomic devices by enclosing the device in a shield of high-permeability material, which attenuates the ambient field and field fluctuations within the enclosure.

The field attenuation for large-scale magnetic shields has been documented in the literature. For five-layer large-scale tabletop shields of roughly 60 cm diameter, a shielding factor of better than $\sim 10^7$ has been reported.⁷ For a constant wall thickness, the shielding factor for a high-permeability enclosure scales inversely with the size of the shield,⁸ so higher field attenuation would be expected for smaller-diameter shields.

Here we discuss the design and testing of a set of five miniature magnetic shields with a volume of less than 3 cm³. Shielding factors were measured for the longitudinal and transverse directions of these cylindrical shields, both individually and in nested combinations. While the external magnetic field B_{ext} could be measured with a commercial Hall-effect gaussmeter, the limited, enclosed volume of the shields and small internal fields made measuring B_{int} more challenging. We used two independent methods for measuring the internal magnetic field: a commercial miniature magnetoresistive sensor and a chip-scale atomic magnetometer.^{10,11} The results from each method were in good agreement.

In Sec. II we discuss the theory of magnetic shielding and quote formulas for estimating the shielding factor of specific shield designs. Section III describes the design and theoretical shielding factors of the miniature, five-layer nested shields tested in this article. The measurement methods and results are described in Sec. IV. In Sec. V we use

scaling arguments to estimate the fields from residual shield magnetization and thermal currents from published results from large-scale shields. We summarize in Sec. VI by comparing the strengths and weaknesses of each technique for measuring small magnetic fields in a restricted volume.

II. THEORY OF MAGNETIC SHIELDING

The magnetic shielding factor S is defined as the ratio of the field applied to the outside of a shielded volume to the field measured inside the shielded volume,

$$S \equiv \frac{B_{\text{ext}}}{B_{\text{int}}}. \quad (1)$$

In general, it is difficult to calculate the shielding factor for a high-permeability enclosure analytically except for some simple cases. Excellent reviews of the developments of shielding theory can be found in Refs. 8 and 12. Here we summarize some key properties of magnetic shields that are relevant to our experiment.

For a spherical shell, the shielding factor can be exactly expressed as⁸

$$S = \frac{1}{9\mu} \left[(2\mu + 1)(\mu + 2) - 2\frac{v}{V}(\mu - 1)^2 \right], \quad (2)$$

where μ is the permeability of the material and v and V are the volumes contained by the inner and outer surfaces of the shell, respectively. For $\mu \gg 1$ and $t \ll D$, where t is the shield thickness and D is the shield diameter, Eq. (2) reduces to

$$S = 1 + \frac{4\mu t}{3D}. \quad (3)$$

Note from Eq. (2) that $S \rightarrow \frac{2}{9}\mu$ as $V \rightarrow \infty$, which points out the limitation of a single-layer shield. For an upper limit value of $\mu = 30\,000$ for the initial permeability,¹² the asymptotic value of S is only about 6700. In practice, we can exceed this limiting value by constructing multilayered shields, where

the resulting shielding factor of a series of nested shields is proportional to the products of the individual shielding factors multiplied by some geometrical scaling factors that approach unity for large intershield spacings. Note that the shield permeability is a nonlinear function of the magnetization and increases to a maximum value of $\mu_{\max} > 400\,000$ at higher applied fields. “Shaking” the shields by continuously applying an alternating magnetic field is a way to take advantage of μ_{\max} .^{13,14}

For cylindrical shells, simple solutions for the shielding factor can be found only for the unrealistic case of a cylinder of infinite length. Solving for cylindrical shells of finite length becomes much more difficult, especially in the longitudinal direction. A cylinder is a practical geometry to construct from sheet metal, so it is a common shape for magnetic shields, and since the longitudinal shielding factor for a cylindrical shield is always smaller than the transverse shielding factor, sometimes by a factor of 10, it usually limits the performance of a magnetic shield. As a result, significant work has gone into calculating longitudinal shielding factors for finite-length cylindrical shells.^{12,15,16} Analytical theoretical estimates of S for cylindrical shields can be found by using ellipsoids to approximate the geometry of a cylinder.^{12,16}

If the shield wall is thin compared to the shield diameter and the permeability is very large, quite accurate estimates of the shielding factor of a series of n shield layers can be found by using the simple approximate expression^{8,9}

$$S_{\text{tot}} = S_n \prod_{i=1}^{n-1} S_i \left[1 - \left(\frac{D_{i+1}}{D_i} \right)^k \right]. \quad (4)$$

Here k depends on the shield geometry. For spherical shells $k=3$, while for cylindrical shells $k=2$ for the transverse shielding factor, and $k=1$ for the longitudinal shielding factor. To within a scaling factor of order unity that depends on the shield geometry,

$$S_i = \mu_i t_i / D_i. \quad (5)$$

Here μ_i , t_i , and D_i are the permeability, thickness, and average diameter of shield layer i , respectively. Note that S_i increases as the diameter of the i th shield decreases, so the shielding factor scales favorably with miniaturization for constant thickness t_i . The advantage of this scaling is illustrated in Fig. 1 with a simple calculation from Eq. (4) of the transverse shielding factor versus shield diameter for various shield combinations.

III. MINISHIELD DESIGN DETAILS

The five-layer, nested magnetic shields were custom made commercially by Amuneal Manufacturing Corporation.¹⁷ The shields were constructed of Amumetal, a high-permeability material comprised of roughly 80% nickel, 15% iron, and a few other elements in smaller amounts. In the earth’s magnetic field, a conservative estimate for μ for this material is 20 000.¹⁸ Note that different companies have different trade names for basically the same material. Five nominally identical sets of shields were manufactured, one of which is shown in Fig. 2. Variations in the dimensions of the

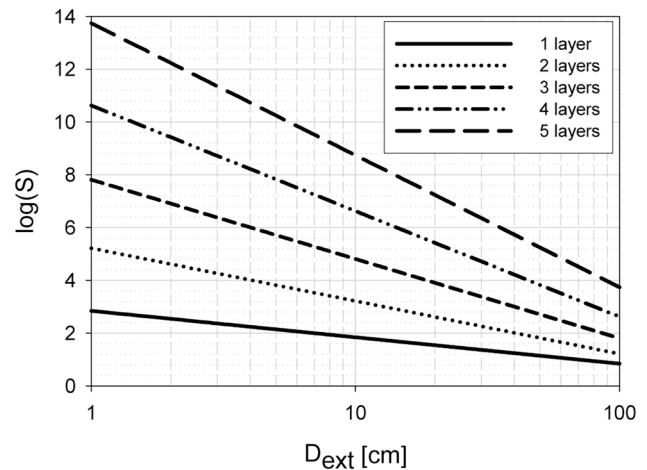


FIG. 1. Calculated transverse shielding factors for magnetic shield combinations of up to five layers vs the diameter of the outermost shield. The thickness of the shielding layers was held constant at $350\ \mu\text{m}$ and a value of $\mu=20\,000$ was assumed. The relative diameters of the five layers are 1:0.85:0.67:0.49:0.32, which corresponds to the geometry of our five-layer shield set. For the multilayer shield calculations, interior layers were added from biggest to smallest.

individual shield layers from the design dimensions were at the level of $100\ \mu\text{m}$. Each shield had a $400\ \mu\text{m}$ hole drilled along the cylindrical axis through the base, and each endcap had two holes, one on axis, of $400\ \mu\text{m}$ diameter, and the other off axis, of $900\ \mu\text{m}$ diameter. The axial holes were used for inserting optical fibers and the off-axis hole for Helmholtz coil or sensor leads. The three smaller layers had an extra set of endcaps with only an axial hole drilled, enabling us to make a rough measurement of the effect of the $900\ \mu\text{m}$ hole on the shielding factor. All shield walls were $350\ \mu\text{m}$ thick.

Table I shows the dimensions and calculated shielding factors of each of the shielding layers and the two combination shields that we studied in detail. S_t is the transverse shielding factor and S_l is the longitudinal shielding factor. Both factors were calculated from Eqs. (4) and (5). Note that the influence of the holes in the ends of the shields is neglected for these calculations.

The penetration of dc fields through the holes would be difficult to calculate accurately, but we expect the effects of the holes to be small. Interestingly, numerical calculations



FIG. 2. (Color online) A set of magnetic shields. The letters can be matched to the data in Table I, which contains the actual shield dimensions. The $400\ \mu\text{m}$ diameter on-axis hole and $900\ \mu\text{m}$ diameter off-axis hole can be seen in each endcap.

TABLE I. Transverse (S_t) and longitudinal (S_l) theoretical and measured shielding factors for each of the individual shield layers (A–E) and two combination shields. The theoretical values were calculated from Eqs.(4) and (5). The calculations assume a sealed cylinder without access holes or removable lids. The measurements of the transverse shielding factors were performed with the atomic magnetometer and the longitudinal shielding measurements were performed with the magnetoresistive sensor. The numbers in parentheses are the standard errors calculated from multiple measurements. The length (L) and diameter (D) of each shield are also given.

Shield layer(s)	L (mm)	D (mm)	S_t (theory)	S_t (expt.)	S_l (theory)	S_l (expt.)
A	19	13	1000	710(1)	360	
B	16	11	1200	918(18)	420	
C	13	8.7	1500	2213(8)	510	
D	10	6.4	2000	1845(7)	650	570(20)
E	7.4	4.1	3000	2154(1)	880	
B and C	16	11	3.5×10^5	$4.6(2) \times 10^5$	2.0×10^4	
B, C, and D	16	11	4.8×10^7	$5.9(1) \times 10^6$	1.7×10^5	$1.9(1) \times 10^5$

have shown that the shielding factor value for a spherical shield with a hole decreases by only a few tens of percent at the center of the shield for holes subtending angles as large as 30° .¹⁹ The largest angle subtended by any of the holes in our shields is 14° (0.9 mm hole in layer E).

Each shield was demagnetized before use^{20,21} by passing the shield by hand through a region of saturating 60 Hz ac magnetic field (30 mT). This demagnetization field was produced with a small coil wound on a bobbin that had an inner diameter approximately equal to the diameter of the largest shield. The shields under test were passed through the coil bobbin and brought out the other side on a time scale of ~ 10 s.

IV. MEASUREMENT METHODS

A. Chip-scale atomic magnetometer

An atomic magnetometer determines magnetic field strength by measuring the Larmor spin precession frequency in a vapor of optically pumped alkali atoms.^{22,23} In a “frequency-modulated Bell-Bloom” configuration²⁵ the magnetic field B is applied perpendicular to a circularly polarized laser beam that is used to both pump and probe the atoms. The frequency of the laser is modulated such that the light spends about half a cycle on resonance, optically pumping the atoms into a state polarized along the direction of the beam propagation, and half off resonance, during which no pumping occurs. When the modulation frequency ω and magnetic field B satisfy the Larmor condition $\omega = 2\pi\gamma B$ (where γ is the gyromagnetic ratio of 3.5 Hz/nT for Cs), a resonant response occurs, creating a large amplitude spin precession about B . This in turn modulates the optical absorption of the medium and hence the intensity of light reaching the photodiode. Passing the photodiode signal to a lock-in amplifier referenced to the driving signal allows the amplitude of the intensity modulation to be extracted, which goes through an extremum when the Larmor resonance condition is satisfied and the atoms are efficiently optically pumped. A full theoretical description of this driven spin system may be derived from Bloch’s equations;²⁴ a useful summary of the theory is given in Ref. 25.

Measuring the magnetic field B_{int} inside a miniature shield requires a small, highly sensitive magnetometer. The

Bell-Bloom magnetometer is well suited to this task for a number of reasons. First, precession is sustained by a modulated optical pumping rate rather than a magnetic driving field, as in the M_x or M_z magnetometer configurations.^{11,23,26,27} The absence of coils for a driving field enables the physics package inside the shields to be simple and small. Secondly, circularly polarized pump light populates an oriented state,²⁸ which remains dark even if the ground and excited state hyperfine structure (9.2 and 1.2 GHz, respectively) is not resolved. This enables us to use a vapor cell with a high N_2 buffer gas pressure of ~ 1 atm. While the high buffer gas pressure produces a collisionally broadened optical linewidth of ~ 18 GHz, it also reduces the rate of relaxing collisions ($1/T_2$) between Cs atoms and the cell walls and hence improves the sensitivity of the magnetometer. (If a higher order atomic polarization moment undergoing Larmor precession were excited, as is done in magnetometers based on nonlinear magneto-optical rotation,²⁹ the upper-state hyperfine structure would have to be resolved.³⁰) One disadvantage of the Bell-Bloom magnetometer is that the magnetic field cannot be measured parallel to the probe beam. Since the optical fiber access holes were drilled only along the cylindrical axes of the shields, we were unable to measure S_l by this technique.

The physics package is shown in Fig. 3. It consists of a vapor cell, a quarter-wave plate and two gradient-index (GRIN) lenses, glued together using optically transparent epoxy, to create a package of length of 7 mm and diameter of 3 mm. The miniature vapor cell contains Cs and 1 atm of N_2 buffer gas. It was microfabricated by etching a 1 mm² hole in a 1 mm thick silicon wafer and sealed by anodically bonding glass wafers to either side.³¹ Such a tiny cell must be heated to create sufficient optical thickness of Cs. Electrical heating currents near the cell would perturb the magnetometer, so the entire shield was placed inside an oven and maintained at $\sim 120^\circ\text{C}$ by hot air from an inline heater. To scan the field inside the shield, a Helmholtz-coil pair was used, which was wrapped around the physics package inside the innermost shield, following a design in Ref. 32.

Light at 895 nm, resonant with the D1 transition in Cs was created with a distributed-feedback diode laser. It was tuned to the atomic resonance with the dc current and modulated on and off resonance with an amplitude of ~ 10 GHz

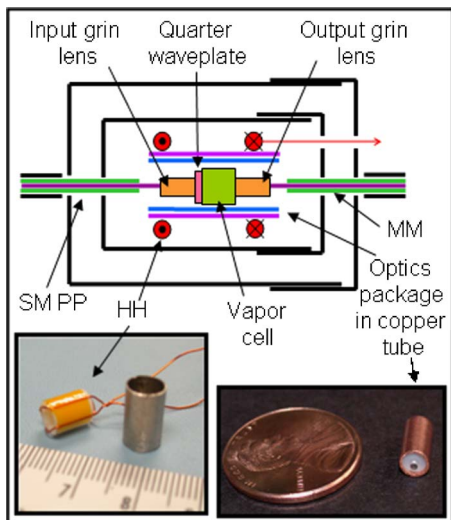


FIG. 3. (Color online) A schematic cross-section diagram (not to scale) of the optics package mounted inside a double-layer shield. Teflon spacers (not shown) maintain the spacing between the shields and support the optics package. The single mode polarization preserving (SM PP) input fiber is shown entering the apparatus from the left and the multimode (MM) output fiber exiting on the right. Both fibers are housed inside a hollow core glass fiber and a hypodermic needle. Inset right: The core optics package mounted inside a copper tube, with a GRIN lens showing. Inset left: Miniature internal Helmholtz coils (HH) mounted on a teflon tube shown next to shield layer “D” (internal coils were only used for multilayer shield measurements).

by applying a square wave to the laser current at a frequency of a few kilohertz. Light was carried into and out of the shield through the axial access holes, by means of a single mode polarization preserving fiber and a multimode fiber, respectively. The fibers were aligned using translation stages that were outside the shields. The shield (with physics package inside) was mounted in the oven and the input fiber was fed into the shield until it butted up against the face of the first GRIN lens. Outside the shield, the fiber was protected from circulating hot air currents by a hollow core glass fiber of $250\ \mu\text{m}$ inner diameter and a stainless-steel hypodermic needle. The GRIN lens was chosen to have its focal point at its input face, so that with the fiber butted against it, it produced a collimated output beam of $\sim 1\ \text{mm}$ diameter that just filled the cell window. Sandwiched between the first lens and the cell was a quarter-wave plate that created circularly polarized light within the cell from the linearly polarized light in the fiber. After light had passed through the cell it was focused by a second identical GRIN lens into a multimode output fiber that was butted against the output lens from the other side of the shield. The polarization properties of the light at the output of the cell are unimportant and we simply want to collect as much of the modulated intensity as possible; hence a multimode fiber with a large numerical aperture is ideal. The output of the photodiode goes to a lock-in amplifier referenced to the pump modulation ω .

Signals such as those in Fig. 4 were seen as the field inside the shield B_{int} was scanned with the internal Helmholtz coils. In Fig. 4 we see resonance peaks at $B_{\text{int}} = \pm\omega/(2\pi\gamma)$ and a central peak at $B_{\text{int}}=0$. This $B=0$ peak occurs because optical pumping can also occur at zero magnetic field with a periodically circularly polarized

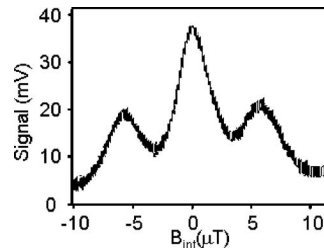


FIG. 4. The peak signal obtained from the lock-in amplifier referenced to the 20 kHz modulation signal. Peaks are seen at $B_{\text{int}}=0$ and at $B_{\text{int}} = \pm\omega/(2\pi\gamma) = \pm 5.7\ \mu\text{T}$.

laser beam. The width of the Larmor resonances is limited by wall collisions and spin-exchange collisions with the nitrogen buffer gas. The shielding factor can be determined from the spectrum by applying a dc offset to the external field and measuring the resulting shift of the peaks. Resonance traces such as Fig. 4 were used to collect a range of information about individual shields: the transverse shielding factor of each of the five layers, variation in S_i between nominally identical shields from different sets, and the effect of the $900\ \mu\text{m}$ hole in the lid.

To enhance the sensitivity of the magnetometer, we also implemented a double-modulation technique. The current through the miniature Helmholtz coils was not only slowly scanned to create a resonance trace but also modulated at 500 Hz. The output of the lock-in amplifier that measured the signal at the 20 kHz laser modulation frequency was fed into a second lock in, which measured the signal at 500 Hz. This second signal was dispersionlike and passed through zero at resonance as the dc field was scanned, as in Fig. 5. The zero signal was independent of drifts in signal size (due to temperature changes, polarization drifts in the fiber, coupling efficiency drifts, etc.) and so longer averaging times could be used to detect field changes of less than 10 nT. The sensitivity of the device was $\sim 20\ \text{nT}/\sqrt{\text{Hz}}$ and was largely limited by the poor collection efficiency of the fiber-coupled detection method. We observed $\sim 70\times$ better sensitivity with the same magnetometer in a larger magnetic shield when the light fell directly onto the photodiode. The degradation of the sensitivity is not fundamental and could be improved in a different design. The fiber-coupled design of our present ap-

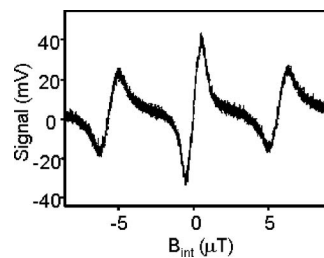


FIG. 5. A dispersionlike signal obtained as the gradient of a peak resonance signal averaged from ten traces. The optical pumping frequency is modulated at 20 kHz and the magnetic field at $B_{\text{int}} = \pm 5.7\ \mu\text{T}$ and also at $B_{\text{int}}=0$. An externally applied field that penetrates the shields causes a shift of the resonances. The transverse value of the penetrating field is measured by compensating the shift of the resonances with an offset current applied to the internal HH coils.

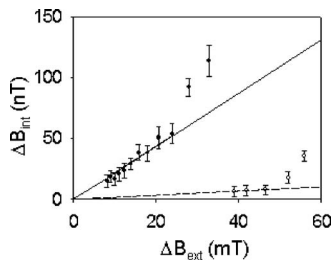


FIG. 6. Plots of ΔB_{int} vs ΔB_{ext} measured using the atomic magnetometer and used to determine S_t for two- and three-layer shields (solid line for closed circles and dashed line for open circles, respectively). Layers B and C were used in both combinations, and D was added for the three-layer shield. The linear fit constrained to pass through the origin was applied to the lowest ten (three) data points from the two-(three-) layer shield where the relationship is linear, to extract the transverse shielding factor. Above that, saturation effects are observed. Note that since the external field is reversed, the applied field is half of the ΔB_{ext} value.

paratus is particularly difficult to align and is also sensitive to vibrations from the forced air heater.

To measure the shielding factor using the double-modulation technique, we applied a calibrated external field with permanent magnets and noted the steady value of I_{int} necessary to zero the signal on the $B=0$ resonance. We then reversed B_{ext} and looked at the change in I_{int} required to re-zero the signal. Using our calibrations, ΔB_{int} and ΔB_{ext} could be calculated and the shielding factor extracted.

The results of measurements of S_t for each shield layer are shown in Table I. The experimental values of S_t are on average 8% less than the theoretical ones, but the level of scatter in the data is larger than the average difference between theory and experiment. We observe a similarly high level of scatter in the measured S_t for all five of the D size shields, using both the single and double-hole lids. The values of S_t for nominally identical shields have a standard deviation of 45%, and the additional hole in the lid reduces S_t by an average of 11%, which is not statistically significant given the scatter in the data. The observed variations in the shielding factor are inconsistent with the small variations in the shield dimensions (less than $100 \mu\text{m}$), and may result from variations in the material permeability arising from either the manufacturing process or subsequent handling of the shields. The theory neglects any effects from the removable endcaps and holes, but our results show that any such effects would change the shielding factor by a few tens of percent or less.

Data for ΔB_{int} vs ΔB_{ext} using two (B and C) and three (B, C, and D) shield layers are shown in Fig. 6 (solid and open circles, respectively). In each case the relationship is linear for low external fields, and saturation effects are evident at higher fields. The solid (dashed) lines are linear fits to the lowest ten (three) points of the two-(three-) shield data constrained to pass through the origin. The inverse of this gradient gives transverse shielding factors of $4.6(2) \times 10^5$ for the two-layer shield and $5.9(1) \times 10^6$ for the three-layer shield. This value of S_t for the three-layer shield is a lower limit, since the large values of B_{ext} that were required to create a measurable B_{int} in the latter case were definitely in the saturation regime. From the dimensions of shield layer “B” and the saturation field value of 0.8 T for Amumetal,¹⁷

we estimate that the shields saturate at an externally applied field of 15 mT. This value corresponds to 30 mT on Fig. 6 because of our field-reversal technique, which is consistent with the data for the two-layer shield. Saturation is confirmed in the three-layer measurement by comparing these experimental results to the theoretical predictions for S_t . The two-layer result is within 30% of the theoretical value of 3.5×10^5 , while for three layers the experimental result is smaller than the prediction of 5×10^7 by a factor of 8.5.

B. Commercial magnetoresistive sensor

The second method for measuring B_{int} used a commercial magnetoresistive sensor. Recall from the above discussion that we were limited to measuring S_t with the atomic magnetometer due to spatial constraints and problems with optical access through the shields. The magnetoresistive sensor had the advantage of allowing us to measure the longitudinal shielding factors relatively easily and quickly. The devices require calibration to produce accurate measurements, however, since the output has a large offset voltage that needs to be subtracted from the measurement. The response can also vary from sensor to sensor and also depends on the sensor’s history.

The device that we used was a Honeywell magnetoresistive sensor,¹⁷ model HMC1052L, together with a simple amplifier. The output of the differential amplifier is given by

$$V_{\text{out}} = g_A \beta V_{\text{cc}} B_{\text{int}}, \quad (6)$$

where $\beta = 1 \text{ mV}/(\text{V G})$ is the response of the magnetoresistive sensor to an applied field, V_{cc} is the bridge voltage, and g_A is the amplifier gain, which we varied from about 100 to 5000, depending on the number of shield layers under study and the expected shielding factor.

We began by measuring the transverse and longitudinal shielding factors for shield layer “D” (the second smallest) by itself. To conduct the measurements, both orthogonal axes of the two-axis magnetoresistive sensor were used. The sensor was aligned such that one sensor axis was parallel and one was perpendicular to the cylinder axis. An external magnetic field was applied to the shield by a pair of permanent magnets and was varied from about 2 to 15 mT at the position of the shield by adjusting the spacing of the magnets. The applied field was measured outside of the shield with a commercial Hall-effect gaussmeter. The shielding factors were then extracted from linear fits to plots of ΔB_{int} vs ΔB_{ext} . For layer D, we measured a transverse shielding factor of $2.5(1) \times 10^3$ and a longitudinal shielding factor of $5.7(2) \times 10^2$. These measurements are both within 25% of the theoretically predicted values, and the value of S_t is also within 25% of the equivalent measurement made with the atomic magnetometer (Table I). The different results from the two measurement methods may result from variations in the sensitivity of the magnetoresistive sensor and/or handling and demagnetization of the shields.

We also measured the longitudinal shielding factor (S_t) for a three-layer shield comprised of layers B, C, and D. Figure 7 is a plot of the measured field inside of the shields versus the applied external field. Saturation effects are clearly visible for ΔB_{ext} greater than 35 mT. Using the un-

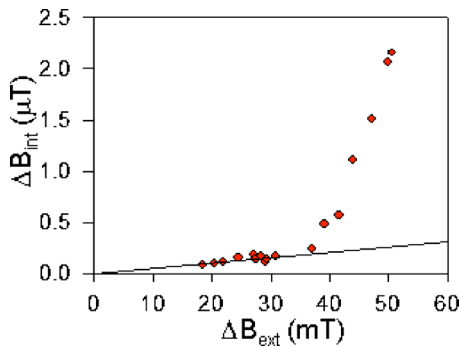


FIG. 7. (Color online) Measurements of the internal longitudinal field vs the externally applied magnetic field for the three-layer B, C, and D shield combination measured using the magnetoresistive sensor. The straight line is a linear fit to the data below 35 mT external applied field, where the measurements are clearly below saturation.

saturated data points we were able to extract a longitudinal shielding factor of $1.9(1) \times 10^5$, in good agreement with the theoretical value of 1.7×10^5 . The range of measured magnetic fields in Fig. 7 corresponds to a range of measured output voltages of about 20 mV. Note that a large offset corresponding to 580 mV has been subtracted from these data. This offset was determined by making a measurement of V_{out} with no applied magnetic field and is only about one tenth of the specified allowable bridge offset voltage for the HMC1052L sensor.¹⁷

The sensitivity of the magnetoresistive sensor was limited in our simple implementation to a level of ~ 100 nT/ $\sqrt{\text{Hz}}$ which gave a field resolution of ~ 35 nT given our measurement time. With this resolution, the sensors could be used only to make accurate measurements of single shields and the longitudinal shielding factor of combinations of shields, which is considerably smaller than the transverse value. Note that we performed dc measurements. In our simple experiment, we traded sensitivity for experimental ease and speed. We could reduce drift and improve the sensitivity by using field coils and a lock-in amplifier to measure field changes at the modulation frequency. The specified noise of the magnetoresistive sensor is 1 nT/ $\sqrt{\text{Hz}}$ at a frequency of 1 kHz.

V. SCALING OF FIELDS FROM RESIDUAL MAGNETIZATION AND THERMAL CURRENTS

Two undesirable effects common to magnetic shields are particularly relevant to compact implementations. The first effect that we consider arises from residual magnetization. In a perfect shield the magnetic domains are very small and randomly oriented, and thus their dipolar fields effectively cancel. In an imperfect shield, there are larger domains whose fields do not cancel. Demagnetizing a shield helps in breaking apart and randomizing these domains, but inside a magnetic shield there is always some small residual magnetic field from this effect. A residual field value from the literature for a large shield of 50 cm diameter is 1 to 2 nT at the shield's center.³³

We observe residual fields of the order of $0.5 \mu\text{T}$ or smaller, and for most of our measurements any residual field was smaller than our measurement resolution. Before we

actually measured the residual fields we were concerned that they could be a big problem because the magnetic field from a dipole falls as the inverse cube of the distance from the dipole. Accounting only for the dipolar dependence and scaling the above experimental result to shields of our size would predict residual fields as large as 2 mT for our compact shields, which is nearly four orders of magnitude larger than what we observe.

It might help to explain this discrepancy if the residual field would also scale with some power of the volume of the innermost shield wall V_{wall} . Scaling the residual field with the dipolar dependence times $V_{\text{wall}}^{1/2}$ predicts a residual field that is at least an order of magnitude larger than what we observe. By scaling the residual field with the dipolar dependence times V_{wall} we find a residual field of the order of 100 nT which is more consistent with our observations. At this time we do not have a good physical model to explain our observations. The residual field for small shields could be a subject of further study.

The other undesirable effect from the shields is thermal currents. Inevitably, thermal currents in conductors generate magnetic field fluctuations that result in field noise. There is a detailed theory^{34,35} on magnetic field noise from thermal currents that agrees well with a tabletop experiment that observed a thermal noise limit of $7 \text{ fT}/\sqrt{\text{Hz}}$ with a shield diameter of 40 cm.³⁶

The theory predicts that the magnetic noise spectrum at a point in space a distance z from current fluctuations in a conducting slab of thickness t is proportional to \sqrt{t}/z . Assuming that we use $t=0.4$ mm for the small shields, scaling the above experimental result would give a field noise of $400 \text{ fT}/\sqrt{\text{Hz}}$. The noise level in our atomic magnetometer experiment was much larger than this value, but higher-performance chip-scale magnetometers are currently performing at noise levels below this limit.³⁷ Lower field-noise limits could be achieved by using a thinner innermost shield or one constructed of ferrite. It has recently been demonstrated that much lower thermal field-noise limits can be achieved in ferrite owing to the higher electrical resistivity of the material.³⁸ Ferrite shields are quite noisy at low frequencies but are nevertheless advantageous in a certain range of frequencies.

VI. SUMMARY

We have designed and tested the shielding factors of sets of five miniature, nested magnetic shields with volumes ranging from 0.01 to 3 cm³. This work has involved measuring small fields in the restricted volume inside each shield, and we have used two independent methods to achieve this. Our shielding factor measurements agree well with estimates calculated from simple theoretical expressions. Using the theory and our measurements for one-, two-, and three-layer shields, we predict that the full five-layer set will have a longitudinal shielding factor of 2×10^9 and a transverse shielding factor of 1×10^{13} . Such shielding performance would attenuate the earth's magnetic field to a level of <50 fT. Higher-performance shielding could potentially be

achieved by making the shields smaller, adding more layers, and/or making the shields more spherical in shape.

ACKNOWLEDGMENTS

The authors gratefully acknowledge advice and technical support from L.-A. Liew, S. Knappe, D. Gallagher, L. Lin, and L. Maltin and thank W. Griffith, M. Lombardi, D. Smith, and J. Stalnaker for helpful comments on this manuscript. This work was supported by the Microsystems Technology Office of the U.S. Defense Advanced Research Projects Agency (DARPA). This work is a contribution of NIST, an agency of the US government, and is not subject to copyright.

- ¹S. Knappe, V. Shah, P. D. D. Schwindt, L. Hollberg, J. Kitching, L.-A. Liew, and J. Moreland, *Appl. Phys. Lett.* **85**, 1460 (2004).
- ²W. J. Riley, *IEEE Trans. Ultrason. Ferroelectr. Freq. Control* **39**, 232 (1992).
- ³Y. Y. Jau, A. B. Post, N. N. Kuzma, A. M. Braun, M. V. Romalis, and W. Happer, *Phys. Rev. Lett.* **92**, 110801 (2004).
- ⁴B. C. Grover, E. Kanegsberg, J. G. Mark, and R. L. Meyer, U.S. Patent No. 4,157,495 (5 June 1979).
- ⁵K. F. Woodman, P. W. Franks, and M. D. Richards, *J. Navigation* **40**, 366 (1987).
- ⁶P. Härle, G. Wäckerle, and M. Mehring, *Appl. Magn. Reson.* **5**, 207 (1993).
- ⁷S. Xu, S. M. Rochester, V. V. Yashchuk, M. H. Donaldson, and D. Budker, *Rev. Sci. Instrum.* **77**, 083106 (2006).
- ⁸A. K. Thomas, *IEEE Trans. Electromagn. Compat.* **10**, 142 (1968).
- ⁹D. Budker, W. Gawlik, D. F. Kimball, S. M. Rochester, V. V. Yashchuk, and A. Weis, *Rev. Mod. Phys.* **74**, 1153 (2002).
- ¹⁰P. D. D. Schwindt, S. Knappe, V. Shah, L. Hollberg, J. Kitching, L.-A. Liew, and J. Moreland, *Appl. Phys. Lett.* **85**, 6409 (2004).
- ¹¹P. D. D. Schwindt, B. Lindseth, S. Knappe, V. Shah, and J. Kitching, *Appl. Phys. Lett.* **90**, 081102 (2007).
- ¹²A. Mager, *IEEE Trans. Magn.* **MAG-6**, 67 (1970).
- ¹³D. Cohen, *Appl. Phys. Lett.* **10**, 67 (1967).
- ¹⁴V. O. Kelhä, R. Peltonen, and B. Rantala, *IEEE Trans. Magn.* **MAG-16**, 575 (1980).
- ¹⁵A. Mager, *J. Appl. Phys.* **39**, 1914 (1968).
- ¹⁶D. U. Gubser, S. A. Wolf, and J. E. Cox, *Rev. Sci. Instrum.* **50**, 751 (1979).
- ¹⁷Products or companies named here are cited only in the interest of complete scientific description and neither constitute nor imply endorsement by NIST or by the US government. Other products may be found to serve just as well.
- ¹⁸L. Maltin, Amuneal Manufacturing Corporation (unpublished).
- ¹⁹T. Rikitake, *J. Geomagn. Geoelectr.* **44**, 919 (1992).
- ²⁰W. B. Herrmannsfeldt and B. L. Salsburg, *Rev. Sci. Instrum.* **35**, 906 (1964).
- ²¹V. O. Kelhä, J. M. Pukki, R. S. Peltonen, A. J. Penttinen, R. J. Ilmonemi, and J. J. Heino, *IEEE Trans. Magn.* **MAG-18**, 260 (1982).
- ²²D. Budker and M. V. Romalis, *Nat. Phys.* **3**, 227 (2007).
- ²³A. L. Bloom, *Appl. Opt.* **1**, 61 (1962).
- ²⁴F. Bloch, *Phys. Rev.* **70**, 460 (1946).
- ²⁵W. E. Bell and A. L. Bloom, *Phys. Rev. Lett.* **6**, 280 (1961).
- ²⁶S. Groeger, G. Bison, J.-L. Schenker, R. Wynands, and A. Weis, *Eur. Phys. J. D* **38**, 239 (2006).
- ²⁷E. B. Aleksandrov, M. V. Balabas, A. K. Vershovskii, A. E. Ivanov, N. N. Yakobson, V. L. Velichanskii, and N. N. Senkov, *Opt. Spectrosc.* **78**, 325 (1995).
- ²⁸A. Kastler, *J. Phys. Radium* **11**, 255 (1950).
- ²⁹D. Budker, D. F. Kimball, V. V. Yashchuk, and M. Zolotarev, *Phys. Rev. A* **65**, 055403 (2002).
- ³⁰J. S. Guzman, A. Wojciechowski, J. E. Stalnaker, K. Tsigtukin, V. V. Yashchuk, and D. Budker, *Phys. Rev. A* **74**, 153415 (2006).
- ³¹L.-A. Liew, J. Moreland, and V. Gerginov, *Appl. Phys. Lett.* **90**, 114106 (2007).
- ³²H. E. Williams, U.S. Patent No. 4,063,207 (13 December 1977).
- ³³J. C. Schouten, A. D. Caplin, C. N. Guy, M. Hardiman, M. Koratzinos, and S. S. Steer, *J. Phys. E* **20**, 850 (1987).
- ³⁴C. T. Munger, *Phys. Rev. A* **72**, 012506 (2005).
- ³⁵J. Nenonen, J. Montonen, and T. Katila, *Rev. Sci. Instrum.* **67**, 2397 (1996).
- ³⁶I. K. Kominis, T. W. Kornack, J. C. Allred, and M. V. Romalis, *Nature (London)* **422**, 596 (2003).
- ³⁷V. Shah, S. Knappe, P. D. D. Schwindt, L. Hollberg, and J. Kitching, *Nat. Photonics* (submitted).
- ³⁸T. W. Kornack, S. J. Smullin, S. K. Lee, and M. V. Romalis, *Appl. Phys. Lett.* **90**, 223501 (2007).